Available online at www.sciencedirect.com
ScienceDirect
Journal of Sound and Vibration 324 (2009) 640–665
JOURNAL OF SOUND AND VIBRATION
www.elsevier.com/locate/jsvi

Earthquake response analysis of RC bridges using simplified modeling approaches

Do Hyung Lee[a,1], Dookie Kim[b], Taehyo Park[c,*]

[a]Department of Civil, Environmental and Railroad Engineering, Paichai University, Daejeon 302-735, South Korea
[b]Department of Civil Engineering, Kunsan National University, Kunsan, Jeonbuk 573-701, South Korea
[c]Department of Civil Engineering, Hanyang University, 17 Haengdang-dong, Seoul 133-791, South Korea

Received 18 March 2008; received in revised form 20 September 2008; accepted 6 February 2009
Handling Editor: L.G. Tham
Available online 25 March 2009

Abstract

In this paper, simplified modeling approaches describing the hysteretic behavior of reinforced concrete bridge piers are proposed. For this purpose, flexure–axial and shear–axial interaction models are developed and implemented into a nonlinear finite element analysis program. Comparative verifications for reinforced concrete columns prove that the analytical predictions obtained with the new formulations show good correlation with experimental results under various levels of axial forces and section types. In addition, analytical correlation studies for the inelastic earthquake response of reinforced concrete bridge structures are also carried out using the simplified modeling approaches. Relatively good agreement is observed in the results between the current modeling approach and the elaborated fiber models. It is thus encouraging that the present developments and approaches are capable of identifying the contribution of deformation mechanisms correctly. Subsequently, the present developments can be used as a simple yet effective tool for the deformation capacity evaluation of reinforced concrete columns in general and reinforced concrete bridge piers in particular.

1. Introduction

The San Fernando earthquake of 1971 has been said to be a major turning point in the development of seismic design provisions for bridges. Subsequently, significant advances in both design practice and analytical schemes have been made. However, although salient improvements have been achieved since then, there are still many aspects of uncertainties in the understanding of the seismic behavior of bridges. Bridges constructed from reinforced concrete have not performed as well as expected under previous earthquake events. In recent earthquakes, particularly the 1989 Loma Prieta, the 1995 Hyogo-Ken Nanbu earthquakes, modern bridges designed for seismic resistance have collapsed or have been severely damaged [1,2]. Such severe failures occurred primarily in the bridge piers.

*Corresponding author. Tel.: +82 2 2220 0321; fax: +82 2 2293 9977.
E-mail addresses: dohlee@pcu.ac.kr (D.H. Lee), kim2kie@kunsan.ac.kr (D. Kim), cepark@hanyang.ac.kr (T. Park).
[1]Tel.: +82 42 520 5571; fax: +82 42 525 7486.

0022-460X/$ - see front matter © 2009 Elsevier Ltd. All rights reserved.
doi:10.1016/j.jsv.2009.02.008

It has been understood that it is not economical design for a bridge to resist a moderate or severe earthquake elastically. Accordingly, bridge piers as a primary source of energy dissipation are generally designed to experience the forces exceeding the yield capacity of the members. This allows potential plastic hinge zones to occur in the piers. Therefore, the seismic response of the bridge structures can be significantly affected by the hysteretic characteristics of the members. Consequently, realistic hysteretic models are developed for the members. Ideally, these models should be derived from sectional material properties. However, the cross-section analysis models are somewhat intensive and are not necessary in the dynamic analysis and global response estimation of large structures [3]. Thus, macroscopic models based on the physical behavior of members have extensively been used in many practical applications in terms of their simplicity and accuracy [4,5]. However, most of the macro models have been derived under constant axial force, and very few macroscopic models that take into account the axial force variation have been proposed. The axial force variation is important since the strengths and deformation capacities [6], particularly shear strengths of reinforced concrete members are largely affected by the varying axial force [7,8]. Works done by Gilbertsen and Moehle [9], Abrams [10], and Saadeghvaziri and Foutch [11] were a few experimental studies among those which considered the axial force variation. Kreger and Linbeck [12] conducted also an experiment in which uncoupled variations of axial and lateral forces were taken into account. However, these works were limited to the response of flexure–axial interaction. Emori and Schnobrich [13], and Keshavarzian and Schnobrich [14] conducted analytical studies in which the effects of fluctuating axial force on the response of RC frame-wall structures were investigated. These analytical studies were also confined to the response of flexure–axial interaction and to proportional axial force variation. Moreover, a single hysteretic model is not deemed enough to approximate the actual behavior of reinforced concrete members, particularly piers, due to the wide range of possible interactions of flexure, shear and axial force during earthquake excitations.

In line of the above, a simple yet effective approach is suggested in the present study. The approach consists of combining macroscopic hinge models to identify the deformation mechanisms of reinforced concrete members. For this approach, axial interaction models (i.e., flexure–axial and shear–axial) have been developed and implemented into a nonlinear finite analysis program. Subsequently, analytical correlation studies with the new models and approaches have been conducted for reinforced concrete column tests. In addition, comparative inelastic time–history analyses have been carried out for RC bridge structures. In the analyses, the bridge structures are modeled by refined fiber elements as well as the current new representations. Then, accuracy and applicability of the present approaches are discussed in comparison with the results of refined fiber elements.

2. Description of hysteretic axial interaction models

The global seismic response of reinforced concrete members can be predicted by two components, which are a primary curve under monotonic loading and hysteretic loops under cyclic loading. In the present work, for both flexure–axial and shear–axial interaction models, the primary curve is represented by a quatrilinear symmetric relationship that considers the cracking, yielding and ultimate states, as illustrated in Fig. 1. In order to define the parameters required for the quatrilinear primary curve, modified compression field theory has been adopted.

Vecchio and Collins [15] proposed the modified compression field theory (referred to as MCFT hereafter) for a reinforced concrete membrane element test in shear. The theory was then extended to predict the response of reinforced concrete members subjected to shear and showed good accuracy [16,17]. Since the theory contains all the salient features sought in the present work for shear in reinforced concrete, it is adopted in the current study. In determining the response of a reinforced concrete member, compatibility, equilibrium, average stress–average strain relationships were employed in the MCFT. Particular emphasis is placed on the concrete material relationship in compression. For cracked concrete in compression in the theory, the constitutive relationship is expressed as follows:

$$f_{c2} = f_{c2\max}\left[2\left(\frac{\varepsilon_2}{\varepsilon_{co}}\right) - \left(\frac{\varepsilon_2}{\varepsilon_{co}}\right)^2\right] \tag{1}$$

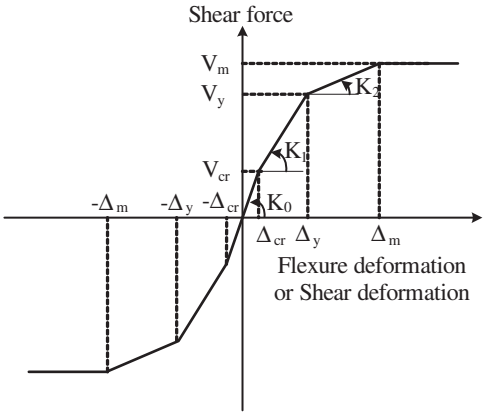

Fig. 1. Quatrilinear symmetric primary curve.

$$\frac{f_{c2\max}}{f'_{co}} = \frac{1}{0.8 - 0.34\varepsilon_1/\varepsilon_{co}} \leqslant 1.0 \tag{2}$$

where f_{c2} is the principal compressive stress, $f_{c2\max}$ is the maximum compressive stress of concrete, ε_{co} is the strain at peak stress of unconfined concrete, f'_{co}, ε_1 and ε_2 are the principal tensile and compressive strains, respectively.

However, the above compressive stress–strain relationship for concrete does not seem to provide an effective confinement to core concrete confined with transverse reinforcement. It is thus modified to include the confinement effect. The work review of both Madas and Elnashai [18] and Martinez-Rueda and Elnashai [19] suggested that the model proposed by Mander et al. [20] was the most promising because of a good balance between simplicity and accuracy and its applicability to various section types. Thus, Mander et al. [20] model has been adopted and implemented into the theory. Hence, the principal compressive stress, f_{c2} is replaced by

$$f_{c2} = v_1 \left[\frac{f'_{cc} xr}{r - 1 + x^r}\right] \tag{3}$$

Parameters in the above expression are given as below.

$$x = \frac{\varepsilon_c}{\varepsilon_{cc}}; \quad \varepsilon_{cc} = \varepsilon_{co}\left[1 + 5\left(\frac{f'_{cc}}{f'_{co}} - 1\right)\right]; \quad r = \frac{E_c}{E_c - E_{sec}}; \quad E_c = 5000\sqrt{f'_{co}}; \quad E_{sec} = \frac{f'_{cc}}{\varepsilon_{cc}}; \quad v_1 = \frac{1}{0.8 - 0.34\varepsilon_1/\varepsilon_{co}}$$

where E_{sec} is the secant elasticity modulus of concrete, ε_{cc} is the strain corresponding to peak stress of confined concrete, f'_{cc} and v_1 is the effectiveness factor.

The remaining conditions of compatibility and equilibrium, and the constitutive relationships for concrete in tension, and both longitudinal and transverse steel reinforcements are kept as those used in the MCFT. A detailed description regarding the MCFT is discussed elsewhere [15]. A computational procedure for the determination of the longitudinal concrete stress is derived based on section analysis procedures suggested by Ang et al. [7] and the complete procedure is described elsewhere [21].

In order to describe the loading, unloading and reloading loops under cyclic loading or earthquakes, a set of hysteretic rules are required. For hysteretic flexure–axial interaction model, the model proposed by Takeda et al. [22] is adopted in the present work. The model has been extensively used for seismic response analysis of reinforced concrete structures and members and shows a good correlation with experimental results [23,24]. For hysteretic shear–axial interaction model, the model proposed by Ozcebe and Saatcioglu [25] is adopted with further modifications and developments. Although the model exhibits good accuracy to test results, the direct application of the model in time–history analysis is uncertain due to the lack of sufficient experimental data. Thus, further developments are of necessary.

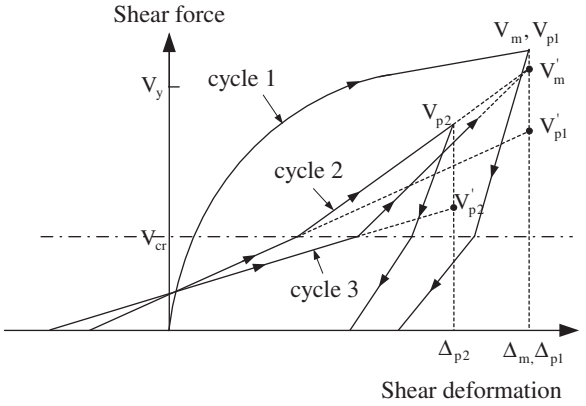

Fig. 2. Example of the reloading branches.

The first development is with regard to reloading stiffness. In the model, reloading stiffness is calculated by the two reference points for the branches below and above the cracking load. The graphical representation of these points and sample reloading branches are shown in Fig. 2.

The coordinates of the two reference points, V'_p and V'_m as shown in Fig. 2 are given by

$$V'_p = V_p e^{\alpha(\Delta_p/\Delta_y)} \tag{4}$$

$$\alpha = 0.82\left(\frac{N}{N_0}\right) - 0.14 < 0.0 \tag{5}$$

$$V'_m = V_m e^{[\beta n + \gamma(\Delta_m/\Delta_y)]} \tag{6}$$

$$\beta = -0.014\sqrt{\frac{\Delta_m}{\Delta_y}} \tag{7}$$

$$\gamma = -0.010\sqrt{n} \tag{8}$$

where V'_p and V_p are the shear force aimed at the previous peak displacement during reloading and the previous peak shear force, respectively; V'_m and V_m are the shear force aimed at the maximum displacement during reloading and the shear force on the primary curve corresponding to maximum displacement; Δ_p is the previous peak displacement; Δ_y is the yield displacement; Δ_m is the maximum displacement; n is a counter; N is the applied axial force; and N_0 is nominal compressive axial capacity based on ACI 318-83 [26].

Reloading stiffness below the cracking load is expressed as a function of both shear displacement ductility and axial force as given in Eqs. (4) and (5). However, since only two levels of compressive axial force (0 and 11 percent of compressive axial capacity based on ACI 318-83 [26]) are used for the development of the model, a relationship for other levels of axial force is of necessary. By using a linear interpolation, other levels of axial force are evaluated and thus Eq. (5) can be replaced by

$$\alpha = 0.055249\left(\frac{N}{N_0}\right) - 0.055251 < 0.0 \tag{9}$$

Since service compressive loads for reinforced concrete bridge columns are generally less than 15 percent of axial compressive capacity [27], the above equation is deemed as an acceptable approximation in the absence of further experimental data. Moreover, if the first unloading point exceeds the cracking load and then the two reference points which define the reloading stiffness are less than the cracking load, reloading stiffness is assumed to follow a straight line targeting the previous unloading point in the direction of loading in order to avoid numerical divergence.

Another salient feature to be considered is the presence of a tensile axial load. Combined with two horizontal ground motion components, the effect of vertical ground motion may lead to an excursion of tensile axial load in bridge columns. However, few experimental data is available regarding reinforced concrete columns subjected to tensile axial load. Maruyama et al. [28] tested a reinforced concrete column with a tensile axial load. The experiment showed that under tension, the crack pattern was dominated by horizontal cracking and diagonal cracking was limited. It also indicated that shear strength deterioration at lower deformation levels was minor but at higher deformation levels it occurred obviously. Based on the above discussion, when tensile axial load is applied, reloading stiffness is assumed to follow a straight line up to the previous peak point in the direction of loading if the cracking load has been exceeded at least once, for the sake of simplicity.

The other assumption is associated with the counter n as given in Eq. (8). During earthquakes, a number of load reversals may occur in a certain maximum deformation range. In this case, the two reference points (Eqs. (4) and (6)) governing the reloading stiffness can be less than the cracking load, which leads to a negative reloading stiffness. Accordingly, the previous points which are not less than the cracking load are used to determine the reloading stiffness in order to avoid such a numerical anomaly.

In addition, further assumption has been made with regard to the unloading stiffness. Shear displacement ductility range between zero and nine was suggested in the original model for unloading stiffness. For irregular structures however, deformation may beyond this ductility range under strong earthquakes. Hence, the unloading stiffness beyond this limit has to be evaluated for the global collapse analysis. For this purpose, the unloading stiffness is assumed to be constant in the case of exceeding the displacement ductility of nine. Thereafter, either flexure or shear failure would have occurred.

The developments and assumptions discussed above are supported by sound engineering judgement and reasonable correlation between analyses and experiments. It is postulated that enhanced improvements may be obtained when more targeted test results become available. More detailed explanation regarding the developments and assumptions is described in Lee and Elnashai [29].

3. Concept for the inclusion of axial force variation

Based on the above primary curve and hysteretic rules, axial interaction models for both flexure and shear are developed. The basic concept in including the effect of axial force variation is that the calculation of stiffness in the current time step is performed by using appropriate shifts corresponding to the current level of axial force between series of primary curves derived for constant axial force levels. These shifts stand for either

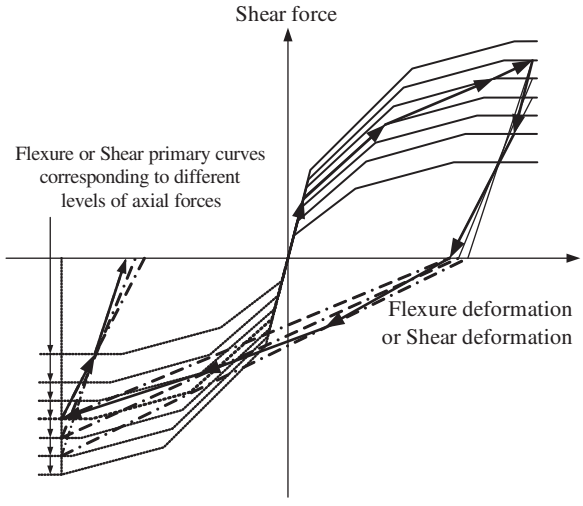

Fig. 3. Graphical representation of stiffness transitions.

hardening (increased stiffness) or softening (decreased stiffness) of a member due to varying axial force. The graphical representation of these shifts for both interaction models is depicted in Fig. 3.

The primary curves are derived for six different levels of constant axial force and thus cracking, yielding and ultimate levels are also shifted in terms of varying levels of axial forces. The primary curves are defined by the user and incorporate three levels in compressive axial force, zero axial force and two levels in tensile axial force. Such an arrangement enables the user with proper selection of axial force range of interest. Hence, consideration of the range of axial force of interest for a particular structure can be made. The primary curve corresponding to an axial force between these pre-specified levels is established within the subroutines implemented using extrapolation. In addition, the axial interaction models incorporate the calculation of force for both a given displacement and the current level of axial force, and updating the stiffness matrix at each incremental step. In order to calculate force and stiffness for varying axial forces, another set of calculation is required. In this calculation, a set of hysteresis loops are traced before start of calculation of force and stiffness in terms of the previous peak points experienced and the current level of axial force. The values of force and displacement corresponding to the previous and current incremental steps are stored and updated in order to achieve the exact location of branches and assure continuity.

4. Program ZeusNL

The hysteretic flexure–axial and shear–axial interaction models are implemented into a nonlinear static and dynamic fiber element analysis program ZeusNL found in Elnashai et al. [30]. ZeusNL has been developed for the nonlinear analysis for 2- and 3-D steel, reinforced concrete and composite structures taking into account the effects of both geometric and material nonlinearities. ZeusNL provides a series of solution strategies. In turn, static, dynamic and eigenvalue solutions are available in the program. Also, availed of are a variety of cross-section types over which a number of monitoring points are divided. In doing so, inelastic response of structural members is accurately accounted for. A detailed description regarding available material models, cross-section types, element types and other solution facilities can be found in Ref. [30].

5. Verification under load reversals

In order to verify the new interaction models, the analytical results obtained with ZeusNL [30] incorporating the new formulations have been compared with experimental results that are available in the literatures. Comparisons have been carried out for reinforced concrete column tests subjected to different levels of constant axial force. It is appreciated that this is not as conclusive as comparisons under varying axial forces. However, in the absence of reinforced concrete column tests subjected to continually varying axial forces, it can be considered as an indirect correlation. Subsequently, earthquake damage observations are employed to validate the general response characteristics of the flexure–axial and shear–axial interaction models under earthquake loadings as discussed later. The test specimens used for the comparisons are divided into two categories, test specimens with flexure-dominated behavior and those with shear-dominated response. With regard to the analytical models, two modeling approaches are utilized for the verification of the new models as illustrated in Fig. 4(a) and (b). Firstly, a single joint element is used to verify the flexure–axial interaction model and hence to evaluate flexural deformation component of flexure-dominated specimens. In this case as shown in Fig. 4(a), the new representation incorporating hysteretic flexure–axial interaction model is applied between two nodes which are initially same. Secondly, two consecutive joint elements are created for the investigation of flexure–shear–axial interaction. As shown in Fig. 4(b), two joint elements are represented by the new formulations governed by hysteretic flexure–axial interaction model and hysteretic shear–axial interaction model. Hence the flexure and shear deformation components can be separately estimated from this modeling approach.

5.1. Flexure–axial interaction model verification

For the verification of the new flexure–axial interaction model, the test specimens with octagonal sections confined with spirals and square sections confined with cross-ties tested by Priestley et al. [31] and Park et al.

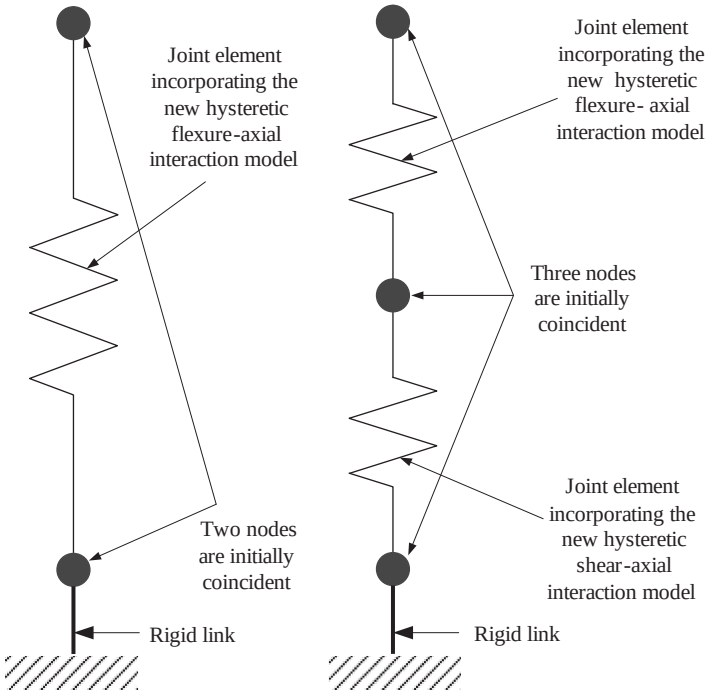

Fig. 4. Simplified analytical modeling: (a) flexure–axial and (b) flexure–shear–axial.

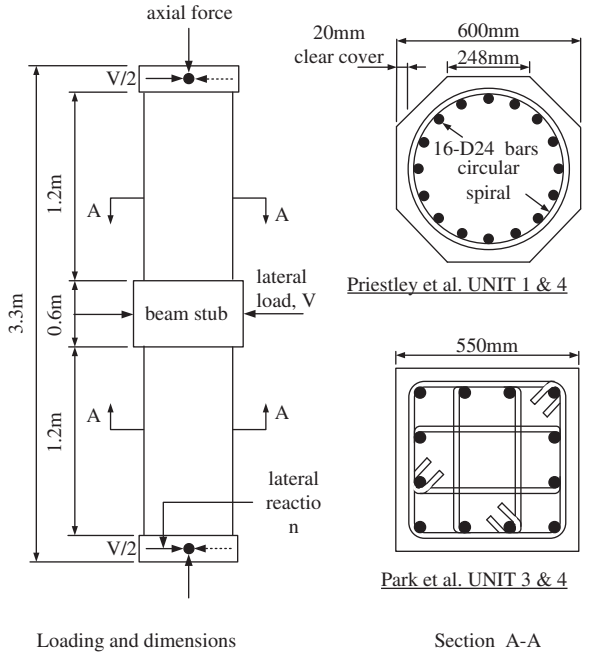

Fig. 5. Details of test specimen.

[32], respectively, have been taken into account. For comparisons with analytical predictions obtained with the new model, two specimens from each test have been selected and used for the verification of the new model. These are UNITS 1 and 4 tested by Priestley et al. [31] and UNITS 3 and 4 tested by Park et al. [32]. Loading condition and cross-sectional dimensions of the specimens are shown in Fig. 5, while the material properties of

the specimens are given in Table 1. As given in Table 1, various levels of applied axial forces and section types are considered for the applicability assessment of the new model.

Fig. 6(a) and (b) shows comparison between the experimental and analytical force–deformation hysteresis loops for specimens UNITS 1 and 4 tested by Priestley et al. [31], respectively. In general, good correlation regarding both strength and stiffness is observed on the overall inelastic response. However, there exist slight differences between analytical predictions and experimental results at higher ductility levels. This may be attributed to bond slip, spalling of the cover concrete and local stress at the cracking location, which are not considered in the present analytical work.

Fig. 7(a) and (b) shows comparison of hysteresis loops for specimens UNITS 3 and 4 tested by Park et al. [32]. The same trends of both strength and stiffness estimation are observed as in the former two cases. Much better correlation would have been obtained if experimental results at higher ductility levels were provided.

Table 1
Material properties and applied axial forces.

Specimen	Concrete strength (MPa)	Axial force (kN)	Longitudinal reinforcement		Transverse reinforcement	
			Ratio[a]	Yield strength (MPa)	Ratio[a]	Yield strength (MPa)
Priestley et al. UNIT 1	28.4	1920	0.0243	303	0.0075	300
Priestley et al. UNIT 4	32.9	3785	0.0243	303	0.0080	423
Park et al. UNIT 3	21.4	2719	0.0179	375	0.0200	297
Park et al. UNIT 4	23.5	4265	0.0179	375	0.0350	294

[a]Ratio indicates the volumetric ratio of reinforcement, i.e., volume of reinforcements/volume of specimen.

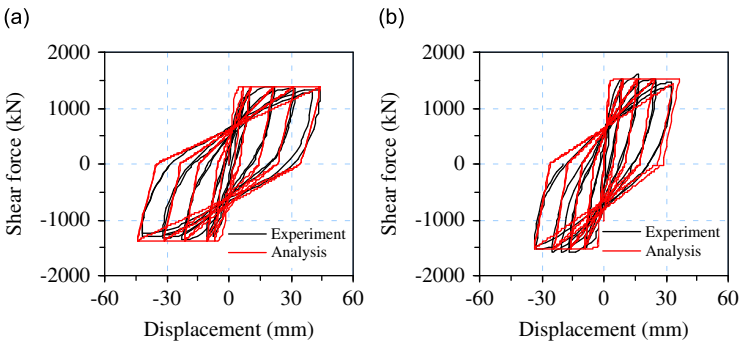

Fig. 6. Comparison of specimens Priestley et al. [31]: (a) UNIT 1 and (b) UNIT 4.

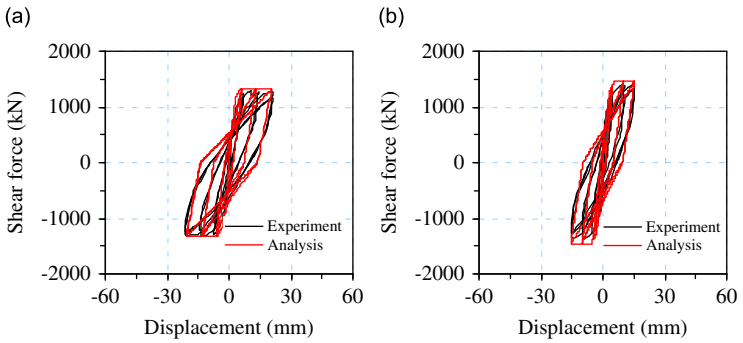

Fig. 7. Comparison of specimens Park et al. [32]: (a) UNIT 3 and (b) UNIT 4.

Table 2
Comparisons of peak strengths at different ductility levels.

Specimen	Peak strength corresponding to each cycle (kN)									
	$\mu = 1$		$\mu = 2$		$\mu = 4$		$\mu = 6$		$\mu = 8$	
	Exp.	Anal.	Exp.	Anal.	Exp.	Anal.	Exp.	Anal.	Exp.	Anal.
Priestley et al. UNIT 1	1180	1380	1337	1380	1373	1380	1344	1380	1328	1380
Priestley et al. UNIT 4	900	1440	1532	1514	1661	1514	1510	1514	1457	1514
Park et al. UNIT 3	567	584	1226	1317	1268	1317	1258	1317	–	–
Park et al. UNIT 4	753	709	1308	1388	1391	1451	1396	1451	–	–

μ Represents displacement ductility factor, i.e., inelastic displacement/yield displacement.

Comparison of peak strengths between analytical predictions and experiments is summarized in Table 2. Test results of Park et al. [32] specimens, UNITS 3 and 4 showed hysteretic response up to displacement ductility factor of 6, while those of Priestley et al. [31] specimens presented the factor of 8. Thus, comparisons of peak strengths have been made up to displacement ductility factor of 6 for Park et al. [32] specimens in Table 2. The difference between experiments and analytical predictions for Priestley et al. [31] specimens UNITS 1 and 4 is large, being 17 and 60 percent, respectively. This difference occurs at displacement ductility of 1 which is elastic limit. This can be due to the fact that, in the test, several elastic cracks at both column surface and the interface between column and footing are formed, and thus early strength and stiffness degradation may occur in elastic range. However, those cracks are not taken into account in the analyses. Nonetheless, the elastic difference does not likely affect the overall response since the most important response is an inelastic one. As observed in Table 2, the difference is decreased at higher ductility levels, hence inelastic range. In all, relatively good agreement is observed within a reasonable margin of 4–12 percent in overall inelastic response.

5.2. *Shear–axial interaction model verification*

Fourteen full-scale tests were conducted by Saatcioglu and Ozcebe [33] to evaluate the response of reinforced concrete columns subjected to slowly applied lateral load reversals. In the test, the column geometry was selected such that the columns were subjected to relatively high shear stresses, although premature shear failure prior to flexural yielding was prevented. Particular emphasis is placed on the specimen U6, the hysteretic shear force–shear deformation response of which has been presented in the work. Subsequently, U6 among the specimens was selected as a representative case. Geometric details and material properties of the specimen U6 are illustrated in Fig. 8(a) and Table 3, respectively. In addition, an experimental study by Maruyama et al. [28] has also been taken into account in the current comparison. A total of 18 specimens were tested including 10 without axial load and 8 with various axial load levels. Fig. 8(b) shows the test specimen which simulates a short square column framing into a relatively stiff floor system. The cross-section represents a 2/3-scale model of a 450 mm column. A 65 mm spacing of transverse reinforcement corresponding to the maximum spacing specified in ACI 318-71 [34] was used so as to ensure that shear behavior dominated. Three test specimens were selected as representative cases. These are OU, 120CU and 100TU subjected to zero, compressive and tensile axial load, respectively. The material properties of the specimens are also given in Table 3.

Fig. 9(a) illustrates the comparison of hysteretic shear force–total deformation response between experiment and analysis with shear. The analysis with shear shows slightly lower response in the initial stiffness than the experiment. This may be due to the piecewise linearization of the shear primary curve. In turn, initial shear stiffness may be underestimated due to the linearization and thus the initial response may be affected by shear. Nevertheless, relatively good correlation is observed in the overall inelastic response.

Comparison between experimental and analytical force–deformation hysteretic behavior of the specimen OU is shown in Fig. 9(b). As observed, the hysteresis loops exhibit a significant pinching. As far as low and medium displacement levels are concerned, the analysis shows relatively good agreement with the experiment

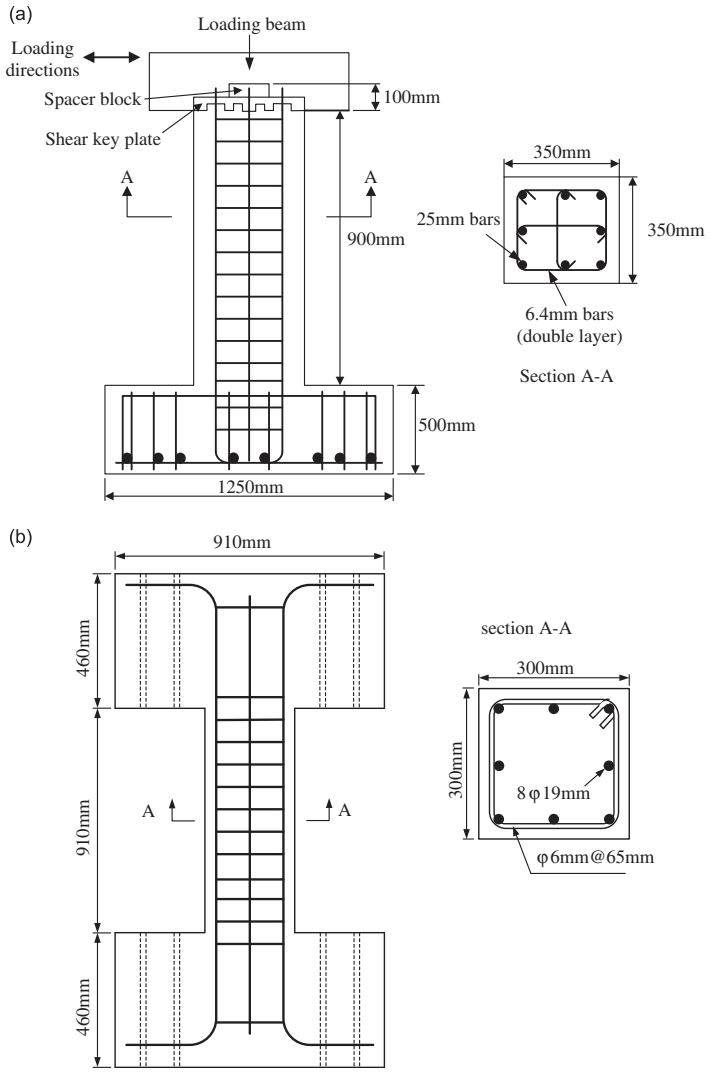

Fig. 8. Geometric details of the specimens: (a) U6 [33] and (b) OU, 120CU and 100TU [28].

Table 3
Material properties of the selected specimens.

Specimen	Concrete strength (MPa)	Axial force (kN)	Yield strength (MPa)	
			Longitudinal reinforcement	Transverse reinforcement
U6	37.3	600	437	425
OU	34.5	0.0	374	466
120CU	30.4	528	450	466
100TU	38.6	−440[a]	374	466

[a] −ve indicates tensile axial load.

in both strength and stiffness. However, the analysis underestimates the strength and stiffness at high levels of displacement. This difference can be attributed to the dependence of the model on the monotonic primary curve (piecewise linear). Fig. 9(c) shows result for specimen 120CU. Since the experimental result provides only the first cycles of loading history, comparison is also made for the first cycles only. In general, a good

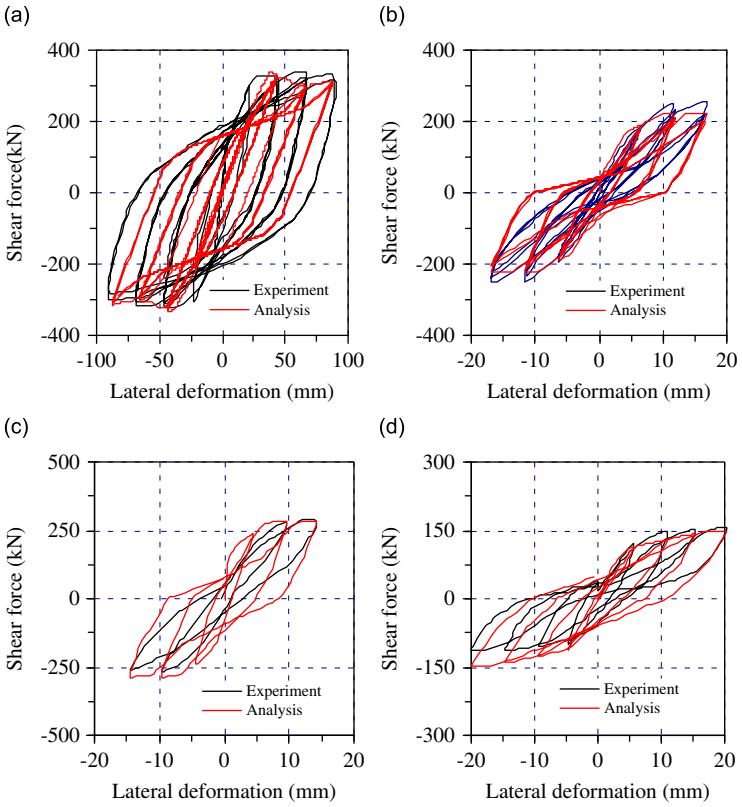

Fig. 9. Comparison of hysteretic response for the specimens: (a) specimen U6; (b) specimen OU; (c) specimen 120CU; and (d) specimen 100TU.

agreement is observed although analytical predictions with shear show somewhat higher unloading stiffness in high displacement levels. Comparison is also undertaken for specimen 100TU and is shown in Fig. 9(d). As in the case of specimen 120CU, only the first cycles are considered. The analytical prediction shows a good result in comparison with test result as illustrated in Fig. 9(d). However, regardless of the symmetric cross-section, the analytical prediction overestimates the strength in the negative direction of loading. This may be due to the asymmetric arrangement in the experiment. Much better agreement would have been obtained if the experimental results are averaged in the two directions.

In short, the accuracy of the new representations is fuelled by the comparisons described above. The above comparative study is not as conclusive as the comparison under varying axial force. However, in the absence of the test data under varying axial force, the present study can be considered as an alternative comparison. Subsequently, inelastic time–history analyses are carried out for reinforced concrete bridges in order to evaluate the further validation and applicability of the developments and are discussed hereafter.

6. Case study 1

In order to validate the new flexure–axial interaction model further, a ramp structure extensively damaged by the 1994 Northridge earthquake is selected. The structure is analyzed for two different models, i.e., the structural model and the lumped hinge model, as shown in Fig. 10. A general layout of the ramp structure is depicted in Fig. 10(a).

6.1. General description of the ramp structure

The deck of the ramp structure consists of a three-celled box girder which is of uniform cross-section along the length of the ramp. The columns of all bents consist of 1219 mm diameter reinforced concrete circular

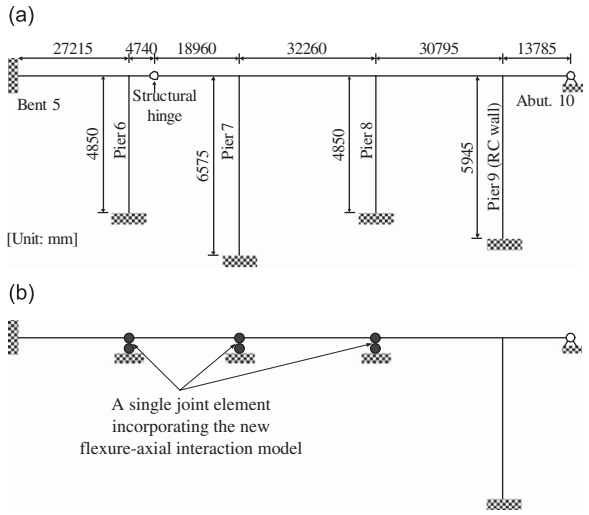

Fig. 10. Analytical models of the ramp structure: (a) structural model (fiber element model) and (b) lumped hinge model.

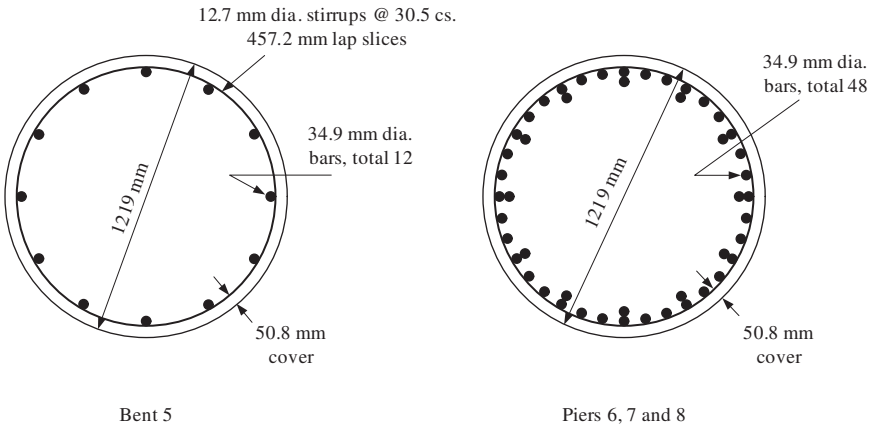

Fig. 11. Cross-section details of piers.

section. Whereas bents 6, 7 and 8 are single columns, bent 5 is composed of three columns. Two columns of bent 5 support this ramp structure and one column of bent 5 supports the adjacent circular off-ramp. Column longitudinal reinforcement is identical for the piers 6, 7 and 8, while less longitudinal reinforcement is employed in the columns of bent 5 as shown in Fig. 11. A detailed description regarding the ramp structure can be found in Broderick et al. [35].

6.2. Analytical modeling of the ramp structure

ZeusNL is used to investigate the earthquake response of the ramp structure. For structural model, five cubic inelastic elements (fiber elements) are employed in the piers, with shorter elements at the base and top of the piers and longer elements toward the center. Such an arrangement allows plastic hinge zones to be accurately captured. Gravity loads are estimated from the cross-sections of deck and piers. Deck is modeled using a cubic inelastic element in each span and the hinge of deck is modeled using a 3-D joint element to allow rotations in the longitudinal and vertical directions. The pier cross-sections are modeled in terms of circular reinforced concrete section available in ZeusNL.

For lumped hinge model, each pier of the ramp structure is replaced by a joint element (point hinge element) representing the new flexure–axial interaction model as shown in Fig. 10(b). Deck is modeled as in the case of the

structural model. Input parameters of the new representation are evaluated using the MCFT. Each pier is analyzed for several levels of constant axial force, 10, 20 and 30 percent of compressive axial force capacity, zero axial force, 10 and 30 percent of tensile axial force capacity (both the capacities were calculated according to ACI 318-02 [36]). Input parameters of the flexure–axial interaction model evaluated using the MCFT are summarized in Table 4.

6.3. Damage description

Whereas no visible damage was inflicted on either the ramp deck or the abutment, pier 6 experienced severe failure and was the most damaged of all the piers supporting the ramp structure. The concrete cover completely spalled over the height and the core concrete disintegrated. Moreover, all the longitudinal reinforcements buckled symmetrically and the transverse hoops opened as illustrated in Fig. 12. It seems that the failure pattern is mainly due to a combination of flexure and axial force and thus the ramp structure is selected for the validation of the new flexure–axial interaction model.

Table 4
Input parameters for flexure–axial interaction model of the ramp structure.

Pier	Limit state	Actions	Compression				Tension	
			0%	10%	20%	30%	10%	30%
Piers 6 and 8	Cracking	Displ. (mm)	1.5	3.5	5.5	8.0	2.5	2.0
		Force (kN)	180.7	406.0	616.6	850.1	94.3	77.4
	Yielding	Displ. (mm)	33.0	32.5	32.1	32.5	33.2	34.2
		Force (kN)	1902	2111	2195	2185	1644	1393
	Ultimate	Displ. (mm)	46.2	42.8	37.1	35.5	46.5	52.7
		Force (kN)	2000	2217	2385	2474	1875	1626
Pier 7	Cracking	Displ. (mm)	3.0	7.0	11.0	15.0	5.0	4.0
		Force (kN)	135.9	318.8	480.0	619.2	75.0	64.0
	Yielding	Displ. (mm)	62.8	62.7	62.2	62.2	63.2	64.5
		Force (kN)	1317	1461	1580	1706	1232	1072
	Ultimate	Displ. (mm)	91.4	77.1	68.8	62.5	97.7	125.4
		Force (kN)	1523	1698	1800	1832	1434	1242

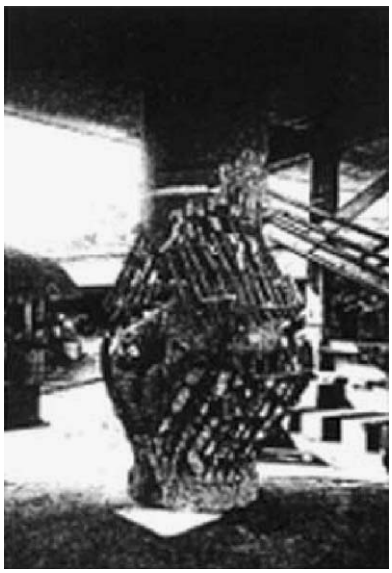

Fig. 12. Damage pattern of pier 6.

6.4. Comparisons of time–history analyses

The input motions employed in the following time–history analyses are accelerograms recorded at the City Hall grounds station in Santa Monica, 1994, approximately 10 km from the location of the ramp structure. Peak ground acceleration is 0.883, 0.346 and 0.230 g for transverse, longitudinal and vertical component, respectively. In order to validate the lumped hinge modeling incorporating the flexure–axial interaction model, comparison of displacement time–history response is made between detailed fiber element model and lumped hinge model. Fig. 13(a)–(c) shows the comparison of transverse displacement time–history response for piers 6, 7 and 8, respectively. Also, shown in Fig. 14(a)–(c) is the comparison of transverse shear force response of the piers between the fiber element model and lumped hinge model. In general, comparison between the two models up to 12 seconds at which single long duration vibration cycle occurred is reasonably good. After 12 seconds, the displacement and shear force response of the lumped hinge model tends to be somewhat greater and lower than those of the fiber element model, respectively. This may be due to lower stiffness characteristics

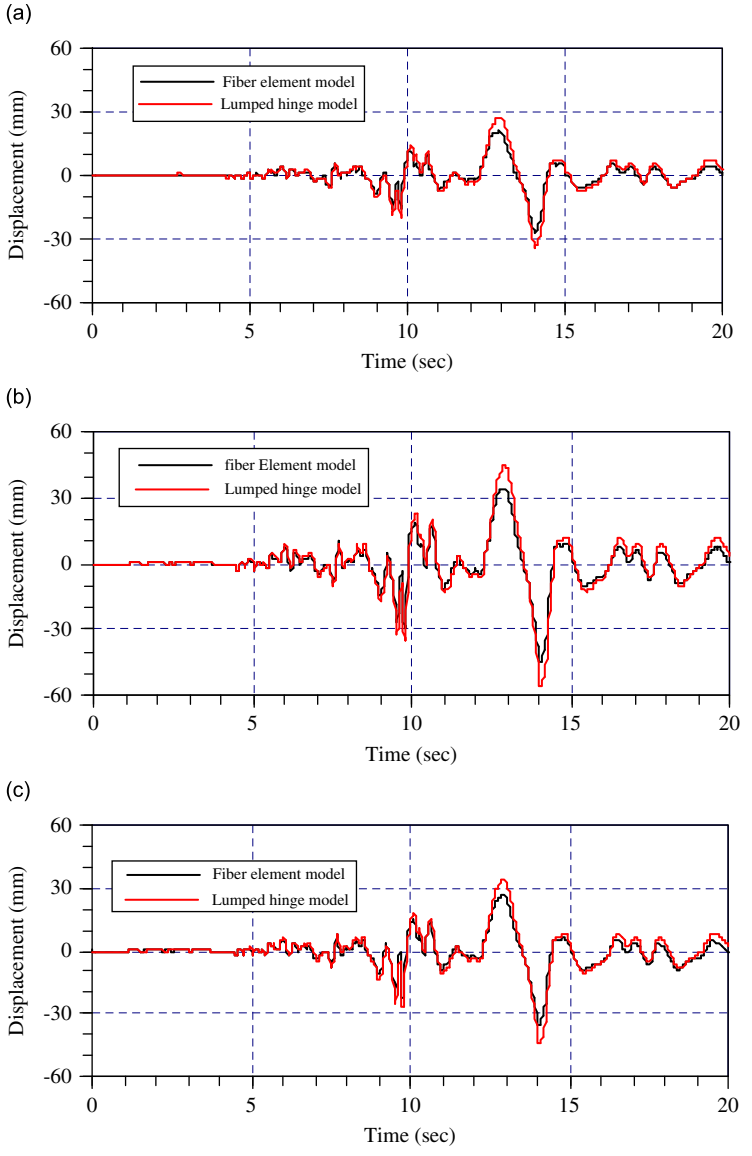

Fig. 13. Transverse displacement response: (a) pier 6; (b) pier 7; and (c) pier 8.

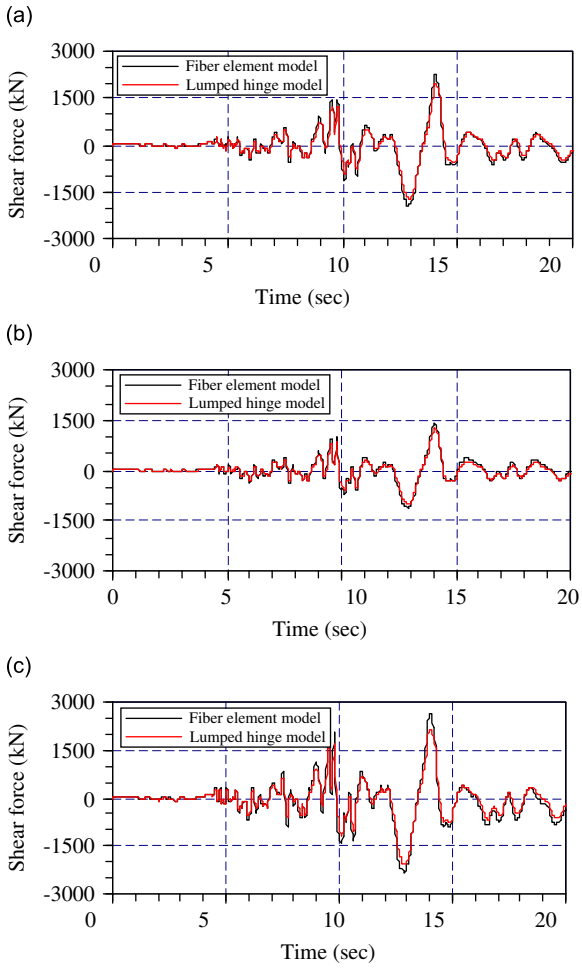

Fig. 14. Transverse shear force response: (a) pier 6; (b) pier 7; and (c) pier 8.

Table 5
Maximum transverse response parameters.

Pier	Fiber element model		Lumped hinge model	
	Displacement (mm)	Shear force (kN)	Displacement (mm)	Shear force (kN)
6	30.63	2026	38.00	1718
7	51.02	1304	62.65	1188
8	40.86	2325	50.60	1808

of the primary curve where the piecewise linear approximation is employed. Nonetheless vibration cycles are nearly identical in both models and hence the period characteristics. Table 5 summarizes the maximum response parameters for both models in the transverse direction.

7. Case study 2

An analytical study of a reinforced concrete bridge severely damaged by the Kobe earthquake of the 17 January 1995 has been carried out for the validation and applicability of the new interaction models developed in the present work. The structure under consideration is a part of the Hanshin Expressway route 3 supported

on single-column bents and two spans of the Expressway supported by the three single piers P663, P664 and P665 are selected and analyzed.

7.1. General description of the Hanshin expressway

The deck of the bridge structure comprises a slab supported on six steel girders seated on fixed and movable bearings. The steel girders are unequal I-sections with different dimensions of top and bottom flanges for external and internal girders. At each pier location, one span is free to slide longitudinally and the other span is fixed along the bridge axis. The pier cross-sections are reinforced concrete circular solid sections of diameter 2300 mm for pier P663 and 2500 mm for piers P664 and P665 and dimensions of piers are shown in Fig. 15(a). Two layers of longitudinal reinforcement are employed for the piers with the inner ring curtailed at mid-height. Pier cross-section details are illustrated in Fig. 15(b). More detailed description regarding the structure can be found in Ref. [37].

7.2. Analytical modeling of the Hanshin expressway

To assess the seismic response of the bridge structure, ZeusNL is again utilized. Three analytical modeling approaches are used to model the bridge structure. For the structural model, two adjacent spans, S662 and S665 (19 and 34 m of span length, respectively) are added in order to accurately reflect the behavior of piers P663 and P665, as shown in Fig. 16(a). In doing so, contribution of forces induced by the two adjacent spans can be reflected in the assessment of the behavior of piers P663 and P665.

Nine cubic inelastic elements are employed for the pier members with shorter elements at the base and longer elements towards the bottom of cap beam to accurately capture possible plastic hinge zones. The pier cross-sections are modeled using circular reinforced concrete section. The deck is modeled by a single steel I-section for each span, with cross-sectional properties to duplicate equivalent bending and torsional stiffness of six steel girders and deck concrete slab, suggested by Part V Seismic Design in Specifications for Highway Bridges published by Japan Road Association [38].

Gravity loads are calculated from the cross-sectional areas of the deck and the piers. Three-dimensional joint elements having three rotational and three translational movements are used at the pier–deck connection. For rotational movements, moment releases around vertical axis and axis perpendicular to bridge axis are employed. For translational movements, longitudinal displacement release is employed for movable bearings, whilst all translation movements are restrained for fixed bearings. The boundary conditions of the two types of bearing are given in Table 6.

The new representations developed in the present work are utilized to simplify the modeling of the bridge structure. Piers P663, P664 and P665 are replaced by a single joint hinge element for the assessment of flexure–axial interaction, whilst two continuous joint hinge elements are utilized for the investigation of flexure–shear–axial interaction. The modeling assumptions and details except for the piers are the same as those in the case of the structural model. The analytical lumped hinge models for flexure–axial and for flexure–shear–axial interaction are illustrated in Fig. 16(b) and (c).

In order to define the input parameters for the new representations of flexure–axial and shear–axial interaction model, each pier is analyzed for six different levels of constant axial force, 5, 10, and 20 percent of compressive axial force capacity, zero axial force, and 10 and 30 percent of tensile axial force capacity. The MCFT is again used for the above analyses. Input parameters from the MCFT are summarized in Tables 7 and 8 for flexure–axial and shear–axial interaction model, respectively. The selection of axial force range is somewhat narrow in lower compression. This is attributed to the fact that the piers are expected to undergo large axial force in compression and thus more accurate axial force variation in compression is required.

7.3. Damage description

Whereas no visible damage occurred in the superstructure of this section, all piers suffered severe damage at mid-height. The concrete cover was completely spalled at mid-height. The core concrete was nearly crushed but has not disintegrated fully. Buckling occurred in most of the longitudinal reinforcement and some of the

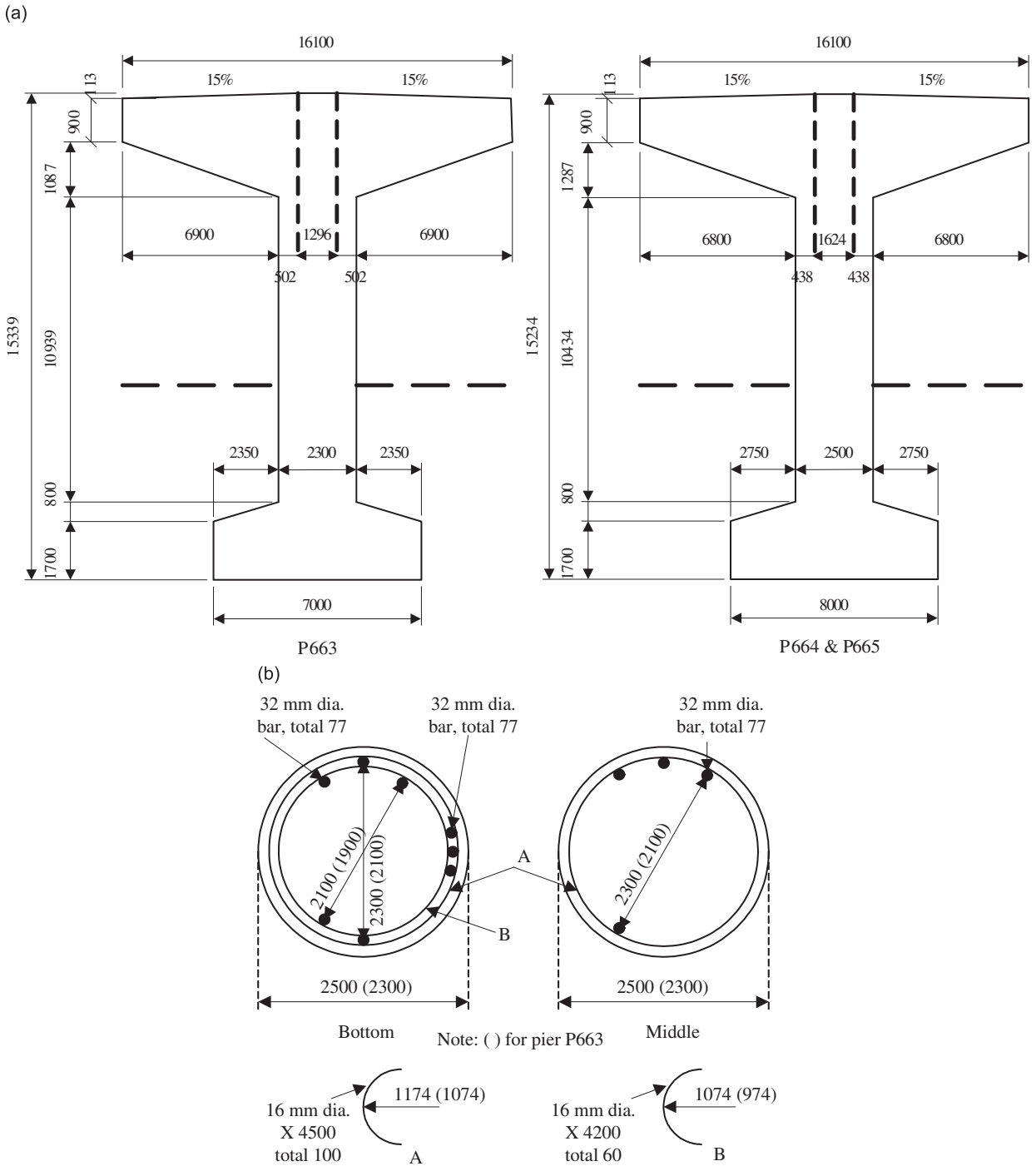

Fig. 15. Details of piers for the Hanshin expressway: (a) dimensions of piers and (c) cross-sections of piers.

confining hoops opened over this height. The typical damage pattern of pier P664 is illustrated in Fig. 17. The damage pattern is not straightforward to attribute to a known mechanism, such as flexural, shear or compression failure. It also cannot be due to lap splicing, as confirmed by the buckled reinforcement. This pattern of damage has motivated the selection of this particular section of the Expressway in order to investigate the applicability assessment of the current developments.

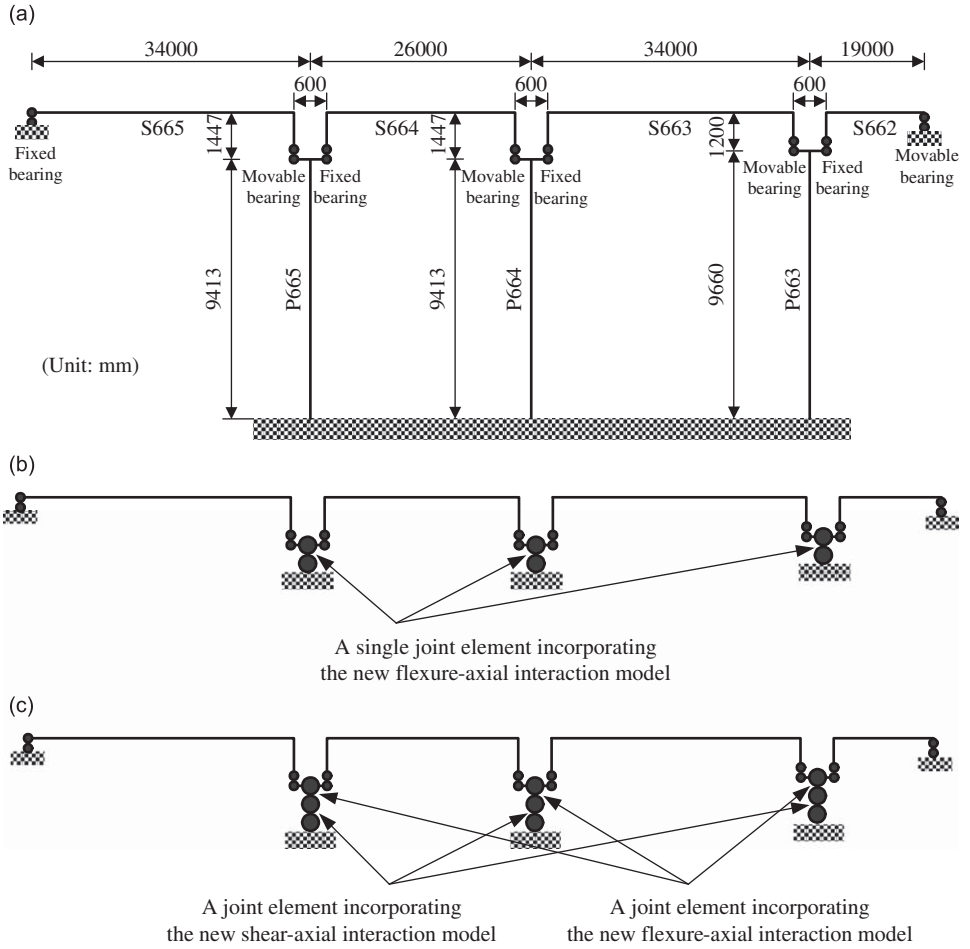

Fig. 16. Analytical models of the Hanshin expressway: (a) structural model (fiber element model); (b) model for flexure–axial interaction; and (c) model for flexure–shear–axial interaction.

Table 6
Boundary conditions of bearings [38].

Bearings	Translational			Rotational		
	Bridge axis	Perpendicular to bridge axis	Vertical axis	Bridge axis	Perpendicular to bridge axis	Vertical axis
Fixed	Elastic	Elastic	Elastic	Elastic	Free	Free
Movable	Free	Elastic	Elastic	Elastic	Free	Free

7.4. Comparisons of time–history analyses

Inelastic time–history analyses are conducted for the three analytical models. Each of the models is analyzed under tri-axial (transverse, longitudinal and vertical) input motions. The input motions employed in the following time–history analyses are the accelerograms recorded at Japan Meteorological Agency (JMA) Kobe station. The corresponding peak ground acceleration was 0.829, 0.632 and 0.341 g for transverse, longitudinal and vertical component, respectively.

Fig. 18 shows comparison of the transverse displacement response between elaborated structural model and lumped flexure–axial interaction model. Whilst the response of the flexure–axial interaction model agrees

Table 7
Input parameters for flexure–axial interaction model of the Hanshin expressway.

Pier	Limit state	Actions	Compression				Tension	
			0%	5%	10%	20%	10%	30%
P663	Cracking	Displ. (mm)	2.0	4.0	7.0	10.0	4.0	9.0
		Force (kN)	526	1043	1680	2414	423	489
	Yielding	Displ. (mm)	39.2	39.8	38.5	38.3	37.3	34.4
		Force (kN)	4974	5733	5988	6546	4708	4100
	Ultimate	Displ. (mm)	56.0	102.3	92.6	80.8	48.0	41.3
		Force (kN)	5706	6455	6824	7512	5225	4518
P664 and P665	Cracking	Displ. (mm)	2.0	3.0	5.0	7.0	3.0	7.0
		Force (kN)	819	1220	1960	2738	469	529
	Yielding	Displ. (mm)	33.7	32.7	31.3	30.5	32.8	28.7
		Force (kN)	6222	6780	7210	7874	5878	5035
	Ultimate	Displ. (mm)	54.6	89.7	75.2	66.8	46.0	35.3
		Force (kN)	6844	7644	8154	9114	6476	5520

Table 8
Input parameters for shear–axial interaction model of the Hanshin expressway.

Pier	Limit state	Actions	Compression				Tension	
			0%	5%	10%	20%	10%	30%
P663	Cracking	Displ. (mm)	0.09	0.23	0.32	0.48	0.10	0.36
		Force (kN)	526	1043	1680	2414	423	489
	Yielding	Displ. (mm)	10.49	9.43	7.83	5.61	10.62	11.33
		Force (kN)	4788	5325	5561	6080	4328	3901
	Ultimate	Displ. (mm)	14.52	14.52	14.17	12.44	15.47	15.30
		Force (kN)	5706	6455	6824	7512	5225	4518
P664 and P665	Cracking	Displ. (mm)	0.12	0.20	0.30	0.44	0.08	0.13
		Force (kN)	819	1220	1960	2738	469	529
	Yielding	Displ. (mm)	10.53	9.04	7.26	5.80	10.73	9.57
		Force (kN)	5834	6358	6549	7477	5464	4706
	Ultimate	Displ. (mm)	15.11	14.58	13.86	13.65	14.77	11.66
		Force (kN)	6844	7644	8154	9114	6476	5520

reasonably well with that of the structural model for pier P663, the response is slightly over-estimated for piers P664 and P665. This can be attributed to the axial forces applied in both piers and linear shifting employed in the analytical model. Piers P664 and P665 carry adjacent longer spans in comparison with pier P663, and thus higher axial forces are applied in piers P664 and P665. This implies that the pronounced axial force variation due to vertical earthquake ground motion is expected in both piers. However, present modeling approach uses six levels of pre-defined axial forces. Subsequently, if axial force varies in between the pre-defined axial force levels, interpolation is made to establish the primary curves. Accordingly, cracking yielding and ultimate levels of primary curves are linearly shifted in terms of varying levels of axial forces. Slight overestimation may thus be due to this linear shifting. Nevertheless, overall vibration cycles are well correlated within an acceptable limit. Fig. 19 illustrates comparison of transverse shear force response. Whereas the transverse shear force response of the structural model shows a single cycle after 8 seconds for all piers, the response of the flexure–axial interaction model predicts two cycles. This may be due to different stiffness characteristics between the structural model and the flexure–axial interaction model where piecewise linear approximation is

Fig. 17. Damage pattern of pier P664.

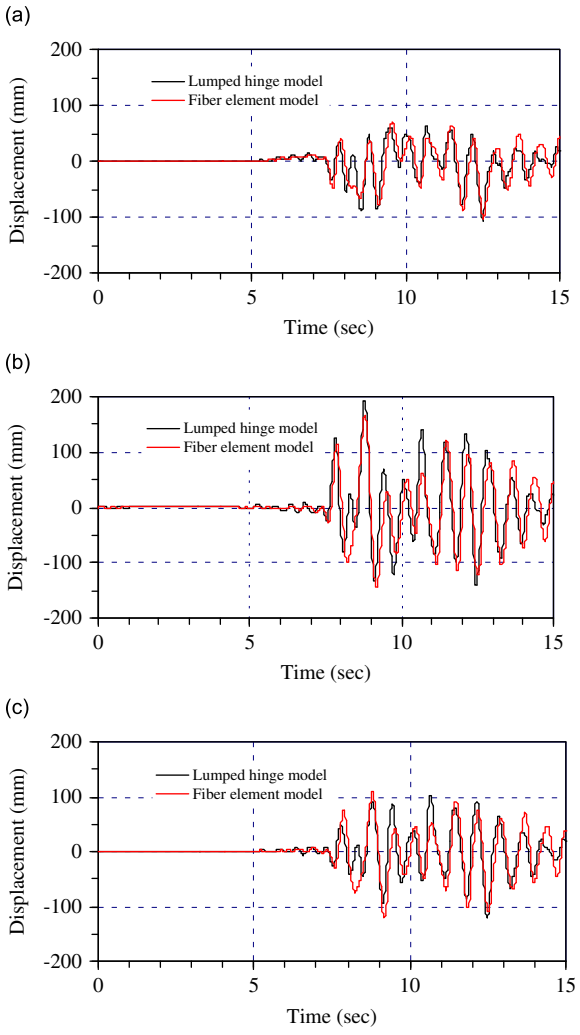

Fig. 18. Transverse displacement response: (a) pier P663; (b) pier P664; and (c) pier P665.

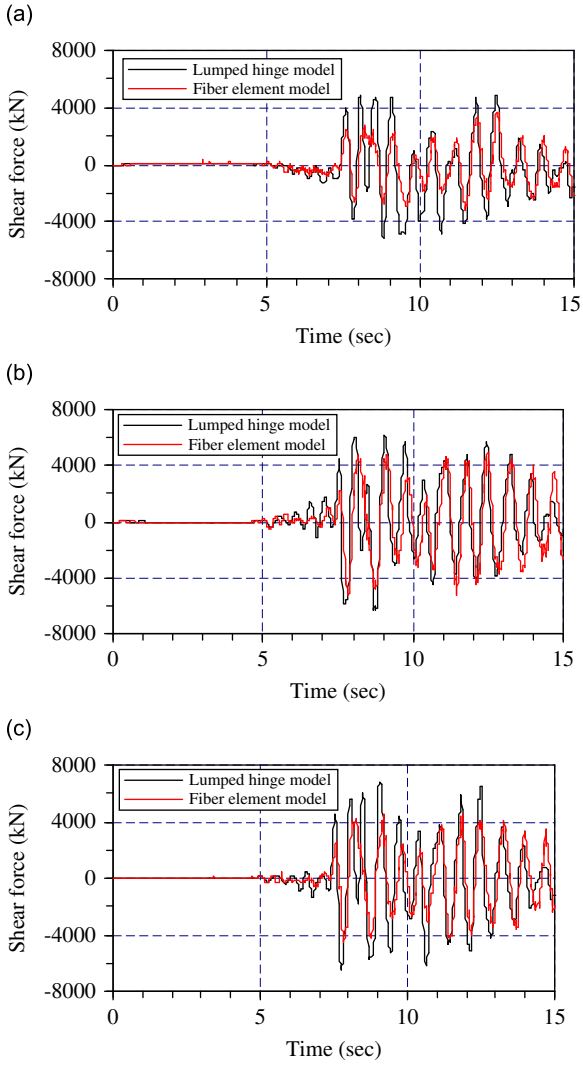

Fig. 19. Transverse shear force response: (a) pier P663; (b) pier P664; and (c) pier P665.

Table 9
Maximum response parameters in the transverse direction.

Pier	Model	Displacement (mm)	Shear force (kN)
P663	Fiber element model	103.0	3656
	Flexure–axial interaction model	106.3	4648
P664	Fiber element model	164.5	4844
	Flexure–axial interaction model	194.0	5826
P665	Fiber element model	108.8	4522
	Flexure–axial interaction model	122.0	5520

employed in the primary curve. Nonetheless, the response after 9 seconds agrees well in terms of vibration cycles, while the response from 11 seconds exhibits a reasonably good correlation in terms of amplitudes. The Maximum response parameters in the transverse direction are summarized in Table 9.

Figs. 20 and 21 depict comparisons of the transverse displacement and shear force response of the lumped hinge models with and without shear. In general, the response of all piers exhibits a minor discrepancy between the model with and without shear in terms of total displacement. However, the response of the pier P664 with shear shows a smaller displacement at 8.8 seconds where the maximum displacement is experienced for flexure–axial response of the P664. This can be explained by the observation of hysteretic response of the pier P664.

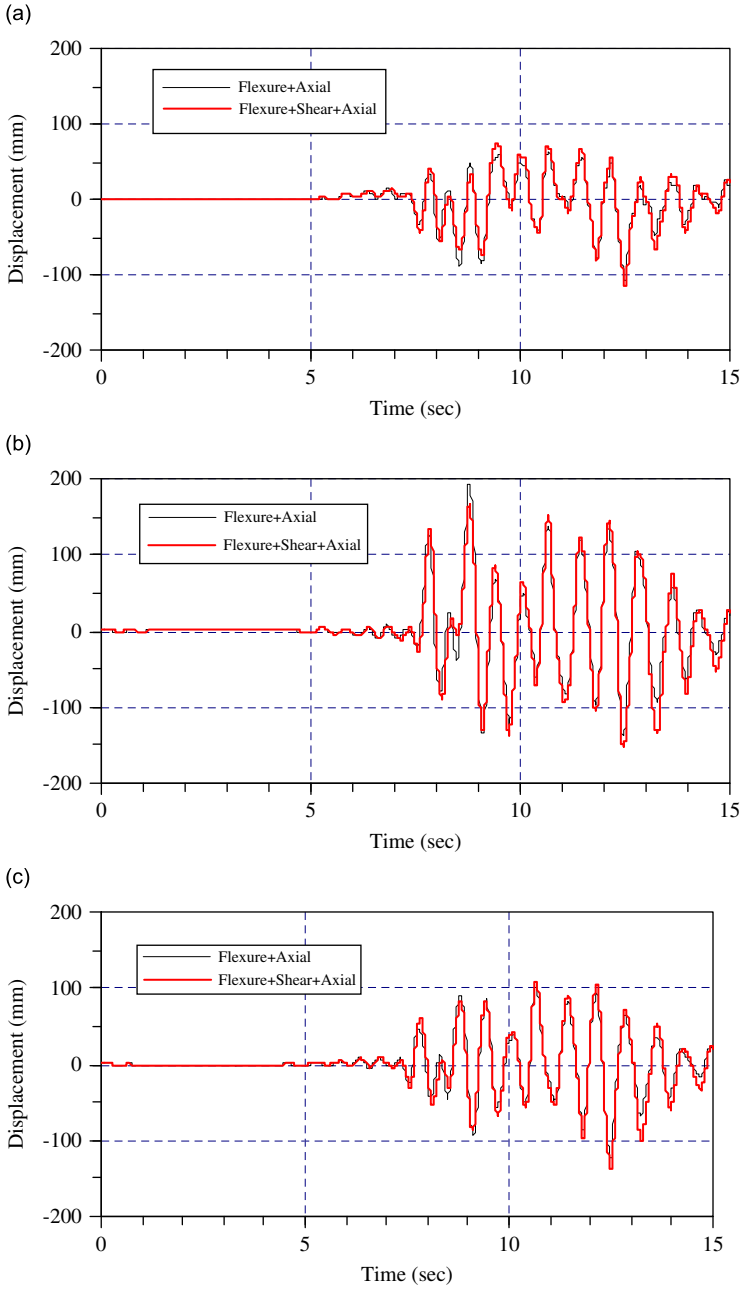

Fig. 20. Transverse displacement response between the model with and without shear: (a) pier P663; (b) pier P664; and (c) pier P665.

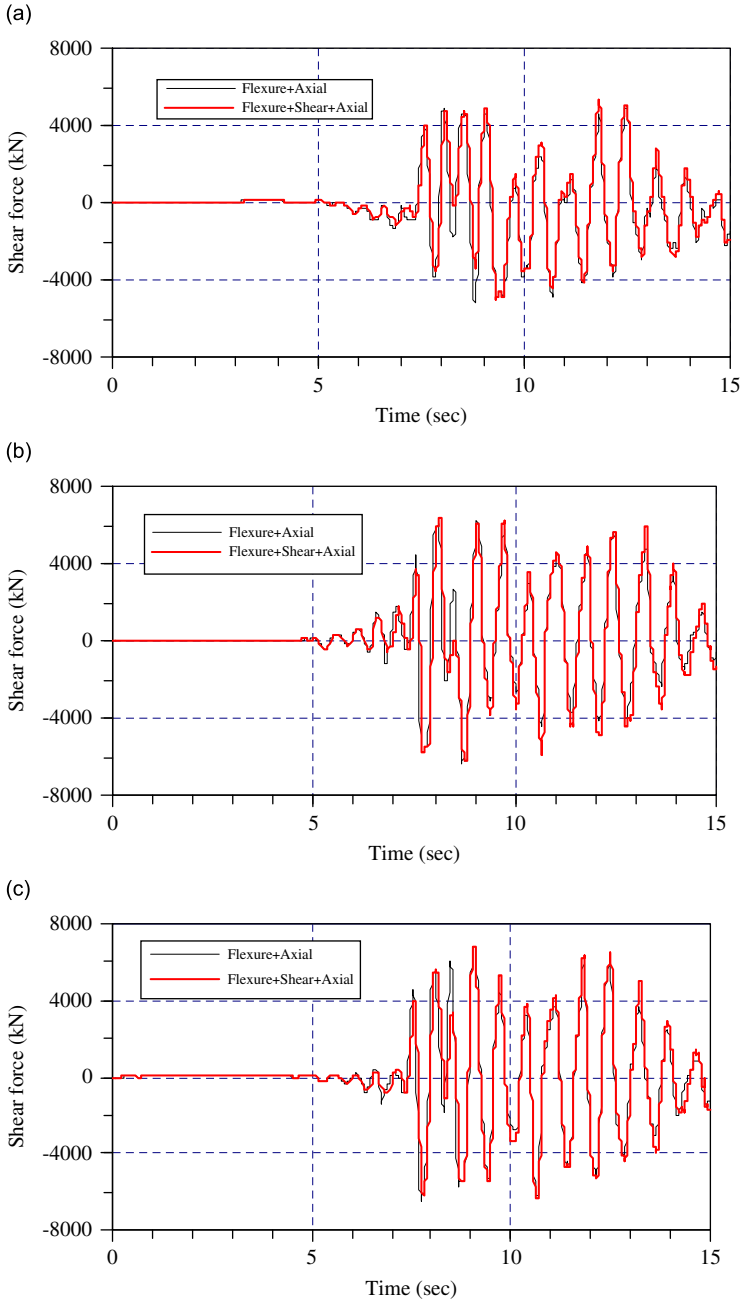

Fig. 21. Transverse shear force response between the model with and without shear: (a) pier P663; (b) pier P664; and (c) pier P665.

Fig. 22 shows comparison of the transverse hysteretic response of the lumped hinge models with and without shear. The flexural response of the pier P664 from the model with shear exhibits a significant reduction in comparison with the flexural response from the model without shear. In addition, pronounced contribution of shear displacement is also observed in the figure. In turn, stiffness degradation due to the inclusion of shear is possibly expected in the pier P664. Also, shown in Fig. 22 is comparison between flexure and shear hysteretic response of pier P664 from the model with shear to investigate the contribution of displacement component on total displacement in the transverse direction. In general, the contribution of shear displacement reaches a considerable level for pier P664. Contribution of flexure and shear displacement

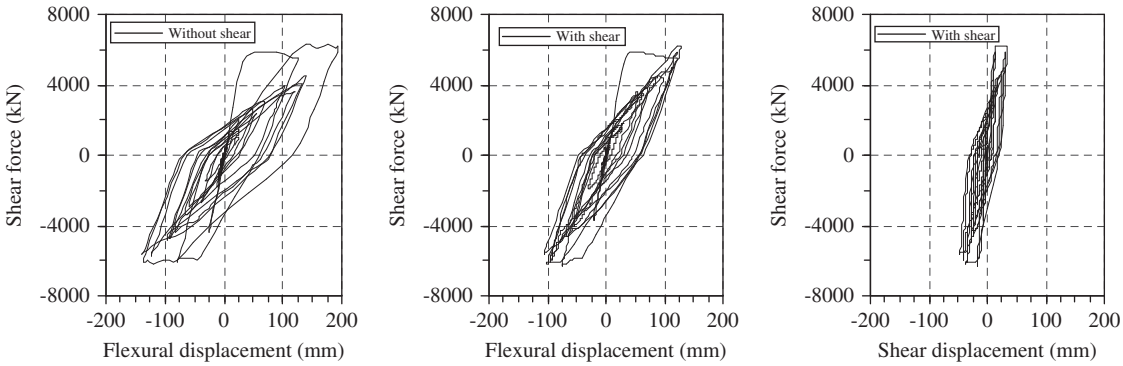

Fig. 22. Comparison of transverse hysteretic response of pier P664.

Table 10
Maximum transverse displacement component.

Pier	Flexure–axial interaction model	Flexure–shear–axial interaction model	
	Flexural displacement (mm)	Flexural displacement (mm)	Shear displacement (mm)
P663	106.3	83.8	28.6 (34.1%)
P664	194.0	129.4	46.3 (35.8%)
P665	122.0	115.6	26.2 (22.7%)

to total displacement is summarized in Table 10. The assessment of maximum response parameters given in Table 10 indicates that shear has a considerable effect on the maximum displacement, being 25, 26 and 19 percent for piers P663, P664 and P665, respectively (meanwhile, the values in parentheses represent the percentage of shear displacement to flexural displacement). It is also noteworthy that flexural displacement in the model with shear is significantly reduced in comparison with that in the model without shear. In other words, considering flexure–axial interaction only may lead to the inaccuracy of displacement capacity and thus produce an erroneous information regarding the stability estimation. This stresses the importance of the current developments. In turn, the present study demonstrates that the response under flexure–shear–axial interaction gives a better explanation with regard to displacement mechanism, and hence damage mechanism.

8. Conclusions

The hysteretic flexure–axial and shear–axial interaction models are developed and implemented into a nonlinear static and dynamic analysis program ZeusNL. Verification of the new models has been undertaken for reinforced concrete columns subjected to different levels of constant axial force since very few reinforced concrete column tests subjected to axial force variation are available. Comparative studies indicate that predicted hysteretic response exhibit good agreement with experimental observation for both flexure-dominated and shear-governing members. Also performed is the seismic correlation study of reinforced concrete bridge structures to establish the validity of the current developments. The results between the lumped hinge models and more elaborated fiber model show relatively good agreement. In addition, the present simple modeling approaches reveal that displacement component may considerably affect on both displacement capacity and stability assessment. It is therefore concluded that the current developments and approaches can be used as a simple yet effective tool for the deformation capacity evaluation of reinforced concrete columns in general and reinforced concrete bridge piers in particular.

Acknowledgment

The work presented in this paper was funded by Center for Concrete Corea (05-CCT-D11), supported by Korea Institute of Construction and Transportation Technology Evaluation and Planning (KICTTEP) under the Ministry of Construction and Transportation (MOCT).

References

[1] A.S. Elnashai, J.J. Bommer, A.Y. Elghazouli, The Loma Prieta (Santa Cruz, California) earthquake of 17 October 1989: seismological, geotechnical and structural field observations, ESEE Research Report No. 89/11, Imperial College London, 1989.
[2] EERI, The Hyogo-Ken Nanbu earthquake, January 17, 1995: Preliminary Reconnaissance Report, Earthquake Engineering Research Institute, Oakland, 1995.
[3] H. Umemura, H. Takizawa, Dynamic response of reinforced concrete buildings, International Association of Bridge and Structural Engineering, Zurich, Switzerland, 1982.
[4] Applied Technology Council, ATC32, Improved seismic design criteria for California bridges: provisional recommendations, 1996.
[5] Federal Emergency Management Agency, FEMA-273, NEHRP guidelines for the seismic rehabilitation of buildings, 1997.
[6] R. Park, T. Paulay, *Reinforced Concrete Structures*, Wiley, New York, 1975.
[7] B.G. Ang, M.J.N. Priestley, T. Paulay, Seismic shear strength of circular reinforced concrete columns, *ACI Structural Journal* 86 (1) (1989) 45–59.
[8] M.J.N. Priestley, R. Verma, Y. Xiao, Seismic shear strength of reinforced concrete columns, *Journal of Structural Engineering, ASCE* 120 (8) (1994) 2310–2329.
[9] N.D. Gilbertsen, J.P. Moehle, Experimental study of small-scale R/C columns subjected to axial and shear force reversals, Civil Engineering Studies SRS 481, University of Illinois at Urbana-Champaign, 1980.
[10] D.P. Abrams, Influence of axial force variations on flexural behaviour of reinforced concrete columns, *ACI Structural Journal* 84 (3) (1987) 246–254.
[11] M.A. Saadeghvaziri, D.A. Foutch, Behaviour of RC columns under nonproportionally varying axial load, *Journal of Structural Engineering, ASCE* 116 (7) (1990) 1835–1856.
[12] M.E. Kreger, L. Linbeck, Behavior of reinforced concrete columns subjected to lateral and axial load reversals, *Proceedings of the Third US National Conference on Earthquake Engineering*, Charleston, August 1986, pp. 24–28.
[13] K. Emori, W.C. Schnobrich, Analysis of reinforced concrete frame-wall structures for strong motion earthquakes, Civil Engineering Studies SRS 457, University of Illinois at Urbana-Champaign, 1978.
[14] M. Keshavarzian, W.C. Schnobrich, Computed nonlinear seismic response of R/C wall-frame structures, Civil Engineering Studies SRS 515, University of Illinois at Urbana-Champaign, 1984.
[15] F.J. Vecchio, M.P. Collins, The modified compression field theory for reinforced concrete elements subjected to shear, *ACI Structural Journal* 83 (2) (1986) 219–231.
[16] S.B. Bhide, M.P. Collins, Influence of axial tension on the shear capacity of reinforced concrete members, *ACI Structural Journal* 86 (5) (1989) 570–581.
[17] F.J. Vecchio, M.B. Emara, Shear deformations in reinforced concrete frames, *ACI Structural Journal* 89 (1) (1992) 46–56.
[18] P.J. Madas, A.S. Elnashai, A new passive confinement model for the analysis of concrete structures subjected to cyclic and transient dynamic loading, *Earthquake Engineering and Structural Dynamics* 21 (1992) 409–431.
[19] J.E. Martinez-Rueda, A.S. Elnashai, Confined concrete model under cyclic loading, *Materials and Structures* 30 (1997) 139–147.
[20] J.B. Mander, M.J.N. Priestley, R. Park, Theoretical stress–strain model for confined concrete, *Journal of Structural Engineering, ASCE* 114 (8) (1988) 1804–1826.
[21] D.H. Lee, Inelastic Seismic Analysis and Behaviour of RC Bridges, PhD Thesis, Imperial College London, 1999.
[22] T. Takeda, M.A. Sozen, N.N. Nielsen, Reinforced concrete response to simulated earthquakes, *Journal of the Structural Division, ASCE* 96 (12) (1970) 2557–2573.
[23] S. Otani, M.A. Sozen, Simulated earthquake tests of R/C frames, *Journal of the Structural Division, ASCE* 100 (3) (1974) 687–701.
[24] T. Takayanagi, W.C. Schnobrich, Non-linear analysis of coupled wall systems, *Earthquake Engineering and Structural Dynamics* 7 (1979) 1–22.
[25] G. Ozcebe, M. Saatcioglu, Hysteretic shear model for reinforced concrete members, *Journal of Structural Engineering, ASCE* 115 (1) (1989) 132–148.
[26] American Concrete Institute, ACI 318-83, Building code requirements for reinforced concrete, 1983.
[27] M.J.N. Priestley, G. Benzoni, Seismic performance of circular columns with low longitudinal reinforced ratios, *ACI Structural Journal* 93 (4) (1996) 474–485.
[28] K. Maruyama, H. Ramirez, J.O. Jirsa, Short RC columns under bilateral load histories, *Journal of Structural Engineering, ASCE* 110 (1) (1984) 120–137.
[29] D.H. Lee, A.S. Elnashai, Seismic analysis of RC bridge columns with flexure–shear interaction, *Journal of Structural Engineering, ASCE* 127 (5) (2001) 546–553.
[30] A.S. Elnashai, V. Papanikolaou, D.H. Lee, ZeusNL—a program for inelastic dynamic analysis of structures, MAE Center, University of Illinois at Urbana-Champaign, USA, 2001.

[31] M.J.N. Priestley, R. Park, R.T. Potangaroa, Ductility of spirally-confined concrete columns, *Journal of the Structural Division, ASCE* 107 (1) (1981) 181–202.
[32] R. Park, M.J.N. Priestley, W.D. Gill, Ductility of square-confined concrete columns, *Journal of the Structural Division, ASCE* 108 (4) (1982) 929–950.
[33] M. Saatcioglu, G. Ozcebe, Response of reinforced concrete columns to simulated seismic loading, *ACI Structural Journal* 86 (1) (1989) 3–12.
[34] American Concrete Institute, ACI 318-71, Building code requirements for reinforced concrete, 1971.
[35] B.M. Broderick, A.S. Elnashai, N.N. Ambraseys, J.M. Barr, R.G. Goodfellow, E.M. Higazy, The Northridge (California) earthquake of 17 January 1994: observations, strong motion and correlative response analyses, ESEE Research Report No. 94/4, Imperial College London, 1994.
[36] American Concrete Institute, ACI 318-02, Building code requirements for structural concrete, 2002.
[37] A.S. Elnashai, J.J. Bommer, C.I. Baron, D.H. Lee, A.I. Salama, Selected engineering seismology and structural engineering studies of the Hyogo-Ken Nanbu (Great Hanshin) earthquake of 17 January 1995, ESEE Research Report No. 95-2, Imperial College London, 1995.
[38] Japan Road Association, Specifications for highway bridges—part V: seismic design 1990, 1990.